ACS APPLIED ELECTRONIC MATERIALS

pubs.acs.org/acsaelm Article

Strain Effects in $SrHfO_3$ Films Grown by Hybrid Molecular Beam Epitaxy

Patrick T. Gemperline,[▽] Arashdeep Singh Thind,[▽] Chunli Tang, George E. Sterbinsky, Boris Kiefer, Wencan Jin, Robert F. Klie,* and Ryan B. Comes*

Cite This: *ACS Appl. Electron. Mater.* 2025, 7, 983−996 Read Online

ACCESS | Metrics & More | Article Recommendations | Supporting Information

ABSTRACT: Perovskite oxide heterostructures host a large number of interesting phenomena such as ferroelectricity, which are often driven by octahedral distortions in the crystal that may induce polarization. $SrHfO_3$ (SHO) is a perovskite oxide with a pseudocubic lattice parameter of 4.08 Å that previous density functional theory (DFT) calculations suggest can be stabilized in a ferroelectric *P4mm* phase when stabilized with sufficient compressive strain. Additionally, it is insulating and possesses a large band gap and a high dielectric constant, making it an ideal candidate for oxide electronic devices. To test the viability of epitaxial strain as a driver of ferroic phase transitions, SHO films were grown by hybrid molecular beam epitaxy (hMBE) with a tetrakis(ethylmethylamino)hafnium(IV) source on $GdScO_3$ and $TbScO_3$ substrates. Strained SHO phases were characterized using X-ray diffraction, X-ray absorption spectroscopy, and scanning transmission electron microscopy to determine the space group of the strained films, with the results compared to those of DFT-optimized models of phase stability versus strain. Contrary to past reports, we find that compressively strained $SrHfO_3$ undergoes octahedral tilt distortions without associated ferroelectric polarization and most likely takes on the *I4/mcm* phase with the $a^0a^0c^-$ tilt pattern.

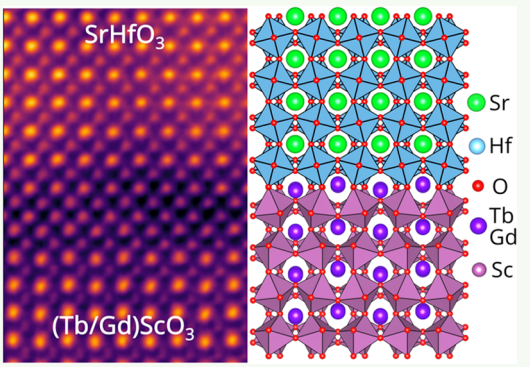

KEYWORDS: *molecular beam epitaxy, perovskite, oxide, strain effects, ferroelectric*

INTRODUCTION

Complex metal perovskite oxides possess a wide range of electrical properties that have made them the focus of many works. They show promise as lead-free piezoelectrics, thermoelectrics, and high κ gate dielectrics in metal-oxide-semiconductor field-effect transistors (MOSFETs). Some of the interesting phenomena are found at interfaces such as two-dimensional electron gas (2DEGs) at $LaAlO_3$ (LAO)/$SrTiO_3$ (STO) interfaces[1] and superconductivity at LAO/$KTaO_3$ interfaces.[2] Perovskite oxides, such as STO and $BaTiO_3$, possess ferroelectric phases and have been investigated as possible materials for ferroelectric field-effect transistors (FeFET) and ferroelectric random access memory (FRAM) devices.[3,4] Good FeFET gate oxide candidates need to be ferroelectric, possess large band gaps, and have high dielectric constants. This has made Hf-based materials such as HfO_2 intriguing due to the unusually weak ferroelectricity observed in the material and the large band gap and dielectric constant that are well known.[5] For these reasons, the demonstration of a hafnate material with a significant ferroelectric response has generated interest in the study of perovskite thin films.

$SrHfO_3$ (SHO) is a perovskite oxide, similar to STO, where corner-sharing HfO_6 octahedra form the building blocks of the three-dimensional framework. The cuboctahedral cavities thus formed by these corner-connected HfO_6 octahedra are filled with Sr cations. SHO exhibits polymorphism and has various energetically competing phases. These phases correspond to space-group symmetries of *Pnma*, *I4/mcm*, *P4/mbm*, *P4mm*, and $Pm\bar{3}m$, where *Pnma* is the ground-state structure. SHO is a large band gap (6.1 eV)[6] perovskite oxide that is orthorhombic (*Pnma*)[7] in the bulk with a pseudocubic lattice constant of 4.08 Å.[6] Temperature-dependent studies have found that SHO can also take on *Cmcm*, *I4/mcm*, and $Pm\bar{3}m$ phases at higher temperatures.[7] Due to its high band gap and high dielectric constant (21),[8] SHO has been investigated as a high-κ gate dielectric for MOSFETs.[9,10] It has also been considered as a possible lead-free piezoelectric material.[11,12]

Unlike other phases of SHO, *P4mm* is noncentrosymmetric, which results primarily from the off-centering of Hf atoms with respect to the center of the HfO_6 octahedra. There have been several theoretical investigations into the possible existence of a polar *P4mm* phase, with several predicting it does not exist[13,14] and others predicting its stability.[11,12] If synthesized,

Received: September 7, 2024
Revised: January 7, 2025
Accepted: January 8, 2025
Published: January 24, 2025

these works predict the *P4mm* phase to be ferroelectric,[13] with a spontaneous polarization of 0.52 C/m^2 along the *c* axis.[11] In the past few years, there have been attempts to synthesize this *P4mm* phase with pulsed laser deposition.[12,15] One study reported the successful synthesis of ∼35 nm-thick *P4mm* SHO films on STO substrates using PLD and found evidence of ferroelectric behavior.[12] However, another study synthesized SHO thin films on STO by PLD and found them to be cubic $Pm\bar{3}m$ and paraelectric.[15] Unfortunately, neither work was able to achieve coherently strained SHO films on STO, where the lattice mismatch is ∼−5%. This indicates that studies exploring films with coherent compressive strain are still needed to understand the viability of a strain-induced polar phase.

A key structural characteristic of a perovskite framework is that the BO_6 octahedra undergo cooperative rotations or tilts. These octahedral tilts are denoted by Glazer's notation.[16,17] Using Glazer's notation, an octahedral tilt pattern can be described as $a^xb^yc^z$, where *a*, *b*, and *c* correspond to the magnitude of the octahedral tilts along those respective crystallographic directions for a pseudocubic unit cell. If the magnitude of the octahedral tilts along two crystallographic directions is equal, then those tilts are denoted by the same symbol. The superscripts (*x*, *y*, and *z*) denote the type of octahedral tilts, where (+) denotes in-phase octahedral tilts for the top and bottom neighboring octahedra, while (−) denotes out-of-phase octahedral tilts. The absence of octahedral tilts along a specific crystallographic direction is denoted by (0). The *Pnma* phase of SHO has an octahedral tilt pattern of $a^+b^-b^-$, the same as those for the $GdScO_3$ (GSO) and $TbScO_3$ (TSO) substrates. The tetragonal phases *I4/mcm* and *P4/mbm* have tilt patterns of $a^0a^0c^-$ and $a^0a^0c^+$, respectively. The *P4mm* and cubic $Pm\bar{3}m$ phases do not exhibit octahedral tilts ($a^0a^0a^0$). Structural models of these phases are shown in Figure S1.

In addition to the possibility of possessing a ferroelectric phase, SHO also shows promise as a dielectric barrier layer in perovskite oxide heterostructures. Certain perovskite oxides, such as $SrNbO_3$, are unstable in the atmosphere or metastable for short periods of time, with exposure causing oxidation of the samples and sample degradation.[18] This problem can be eliminated by adding a capping layer that buries the interfaces. However, this usually involves careful selection of a material based on its electronic and magnetic properties so that it will not affect the samples of interest.[19,20] Density functional theory (DFT) calculations for SHO have predicted that SHO's insulating behavior will prevent it from accepting donor electrons from any other transition metal perovskite oxide.[21] This makes SHO an excellent candidate for capping atmospherically unstable and metastable perovskite oxides, as they would preserve the structure of the films while not changing the electrical properties of the films and interfaces. Theory also predicts that charge transfer through thin layers of SHO would still be possible, allowing for modulation doping of samples and the formation of 2DEGs at heterostructure interfaces.[21] Hafnate materials have been employed as dielectrics to enable $BaSnO_3$ 2D electronic systems for possible device applications,[22,23] where the lattice match is more favorable than other perovskite dielectrics. The development of molecular beam epitaxy (MBE) growth capabilities for SHO is important for interfacial electronic devices that require a good dielectric barrier or capping layer.

A key reason epitaxial SHO has not been synthesized using MBE is due to the refractory nature of Hf. Refractory metals have low vapor pressures even at temperatures approaching 2000 °C. Thus, it is not practical to evaporate these elements in an effusion cell, and an electron-beam evaporation source is needed instead. However, over the past few years, hybrid molecular beam epitaxy (hMBE) has made significant progress in repeatably and reliably utilizing such refractory metals to synthesize perovskite oxides.[18,24−26] hMBE achieves this by utilizing metal organic precursors commonly employed in atomic layer deposition (ALD) as a source material rather than pure metallic sources. Others have proposed the use of oxide sources in effusion cells that may evaporate as suboxide metal-oxide molecules and have proposed HfO as one possible source,[27] but this has not yet been demonstrated and would still require evaporation from sources above 2000 °C. Thus, metal organic precursors with high vapor pressures at considerably lower temperatures offer the most promising avenue for consistent and well-controlled deposition of Hf by MBE. Several Hf precursors are commercially available, but tetrakis(ethylmethylamino)hafnium(IV) was chosen in this work due to its high vapor pressure, common use in atomic layer deposition, and thermal stability.[28]

In this combined experimental and theoretical work, total energy calculations using DFT were carried out over a wide range of compressive and tensile strain to determine the thermodynamic stability of various phases of SHO. To determine the viability of compressive strain to drive phase transitions in SHO, thin film samples of SHO were grown on STO, $TbScO_3$ (TSO, pseudocubic lattice parameter, a_{pc} = 3.954 Å), and $GdScO_3$ (GSO, a_{pc} = 3.963 Å) using hMBE. In situ high-energy electron diffraction (RHEED) was used to monitor the film surface during the growth process, and *in vacuo* X-ray photoelectron spectroscopy (XPS)[29] was used to investigate film composition and stoichiometry. High-resolution X-ray diffraction (HRXRD) and reciprocal space mapping (RSM) were used to determine film relaxation, while scanning transmission electron microscopy (STEM) was used to determine the film's atomic structure and chemical distribution. Four-dimensional scanning transmission electron microscopy (4D-STEM) measurements of the samples were used to evaluate the atomic-scale space group symmetry of the film within the sample. The electronic structure of the film and its dependence on the compressive strain was measured using X-ray absorption spectroscopy (XAS) and compared with the electronic density of states calculations. The presence of polar distortions was investigated using second harmonic generation (SHG). We find that significant compressive strain can be achieved on TSO and GSO substrates leading to a non-equilibrium phase of SHO, but that this phase is nonpolar rather than the ferroelectric *P4mm*, in agreement with our predictions via DFT.

FIRST-PRINCIPLES MODELING

To predict phase stability as a function of epitaxial strain, the thermodynamic ground state for 5 phases of SHO with differing octahedral distortions was calculated using density functional theory (DFT). The computations were performed with the Vienna ab initio Simulation Package[30,31] accounting for electronic exchange and correlations within the Perdew−Burke−Ernzerhof (PBE) parametrization of the generalized gradient approximation (GGA).[32] Electrons are treated within the projector-augmented-wave framework (PAW).[33,34] We followed Material Project recommendations and adopted a plane wave energy cutoff of E_{cut} = 520 eV[35] and a Γ-centered *k*-point grid with a k-spacing of 0.3 Å^{-1}. We examined the

https://doi.org/10.1021/acsaelm.4c01595
ACS Appl. Electron. Mater. 2025, 7, 983−996

following phases: *Pnma*, *I4/mcm*, *P4/mbm*, *Pm$\bar{3}$m*, and *P4mm*. The equilibrium structures were subjected to in-plane strain ranging from −5 to +5% in steps of 0.5% for each phase. The out-of-plane lattice parameter was calculated using the equation $\epsilon_{33} = \frac{-\nu}{1-\nu}(\epsilon_{11} + \epsilon_{22})$. The value of Poisson's ratio (ν) of 0.3 for SHO was determined using lattice parameters obtained from XRD measurements of the samples described below. This value is consistent with the computed Poisson ratio of 0.25 for the *Pm$\bar{3}$m* phase. Other models with different elastic responses are shown in Figures S3−S6. In order to determine the e_g and t_{2g} ordering, we computed the electronic density of states with energy bins of <15 meV. The site-projected eDOS d-orbital angular momentum channels in the d-orbital manifold were computed and normalized to arbitrary units (for phases with more than 1 Hf per uc), providing phase resolved t_{2g} (d_{xy}, d_{xz}, and d_{yz}) and e_g (d_z^2 and $d_{x^2-y^2}$) ordering.

Figure 1 shows the crystal structure and electronic density of states relative to the conduction band minimum (CBM) for

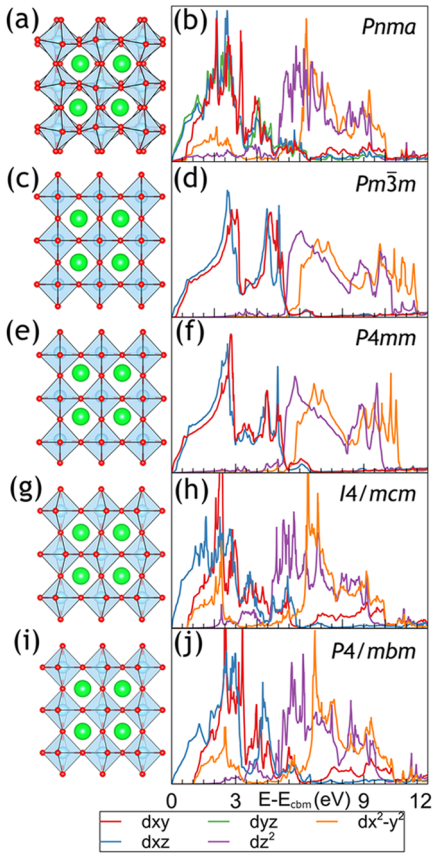

Figure 1. (a), (c), (e), (g), and (i) Show the crystal structure of SHO for −3% in-plane strain for *Pnma*, *Pm$\bar{3}$m*, *P4mm*, *I4/mcm*, and *P4/mbm*, respectively. (b), (d), (f), (h), and (j) Show the eDOS results of our DFT results relative to the conduction band minimum (CBM) for *Pnma*, *Pm$\bar{3}$m*, *P4mm*, *I4/mcm*, and *P4/mbm*, respectively. The d_{xz} and d_{yz} states are degenerate for all phases but *Pnma*.

the insulating *Pnma*, *P4mm*, *Pm$\bar{3}$m*, *I4/mcm*, and *P4/mbm* phases of SHO with −3% compressive in-plane strain. The atomic models along all of the pseudocubic crystallographic axes for SHO and substrates (TSO and GSO) are shown in Figures S1 and S2, respectively. For *P4mm*, we find a small lattice distortion of c/a = 1.002, and that Hf is located above the equatorial plane of the HfO_6 octahedron by 0.08 Å, consistent with a ferroelectric phase. However, we find that the *P4mm* phase is not the ground state. The energies for each phase as a function of the in-plane strain are plotted in Figure 2. The strain was calculated using $f = \frac{a_{substrate} - a_{film}}{a_{film}}$, where the

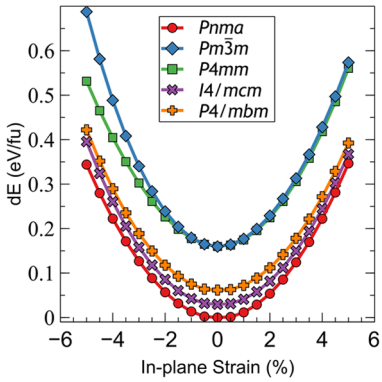

Figure 2. Plot of the change in energy from the ground state for the different SHO phases as a function of in-plane strain.

pseudocubic lattice constant and bulk lattice constant were used for the substrate and film, respectively. From Figure 2, we observe that *Pnma*-structured SHO is the thermodynamic ground state, consistent with previous computations[12] and experiment.[7] *Pnma* remains the structural ground state for compressive and tensile strain in the range from −5 to +5%, covering the range of feasible strain values and experimental values. We find that phase stability decreases in the order *Pnma* (0 eV/fu) < *I4/mcm* (30 meV/fu) < *P4/mbm* (62 meV/fu) < *P4mm* (160 meV/fu) ∼ *Pm$\bar{3}$m* (160 meV/fu) at 0% strain, consistent with previous work.[12] We note that the *P4mm* and *Pm$\bar{3}$m* equilibrium structures are energetically degenerate but structurally distinct. At −3% compressive strain, we find that phase stability decreases in the order *Pnma* (127 meV/fu) < *I4/mcm* (158 meV/fu) < *P4/mbm* (189 meV/fu) < *P4mm* (303 meV/fu) ∼ *Pm$\bar{3}$m* (340 meV/fu). Furthermore, we have also investigated the impact of strain on the thermodynamic stability of different SHO phases by (1) keeping ϵ_{33} constant at 0.0 while varying ϵ_{11} and ϵ_{22} and (2) calculating ϵ_{33} with a constant unit cell volume. Those results are summarized in Figures S3−S6.

EXPERIMENTAL METHODS

Hybrid MBE. SHO films were grown in a (001) orientation on (110)-oriented GSO and TSO with pseudocubic lattice parameters of 3.963 and 3.954 Å, respectively, and on STO with a lattice parameter of 3.905 Å. While GSO and TSO have nonequivalent in-plane lattice parameters due to their orthorhombic structures, the differences between their pseudocubic lattice parameters are greater than the inhomogeneity on the substrate surface. Thus, we believe that any variations between samples can be explained by epitaxial strain rather than inhomogeneous in-plane strain due to the substrate. Substrates were obtained from MTI Crystal and sonicated in acetone and then in isopropanol before being dried with nitrogen. GSO and TSO substrates were annealed for 6 h at 1100 °C in a Lindberg Blue M tube furnace from Thermo Scientific. A Park Systems Atomic Force Microscope (AFM) was used to confirm that this treatment resulted in a single termination with step edges of ∼200 nm in width. All samples were grown in a Mantis MBE. The substrates were heated to 1000 °C over 1 h in an oxygen plasma with a pressure of 2×10^{-6} Torr to prevent the surface of the substrate from reducing before growth.

https://doi.org/10.1021/acsaelm.4c01595
ACS Appl. Electron. Mater. 2025, 7, 983−996

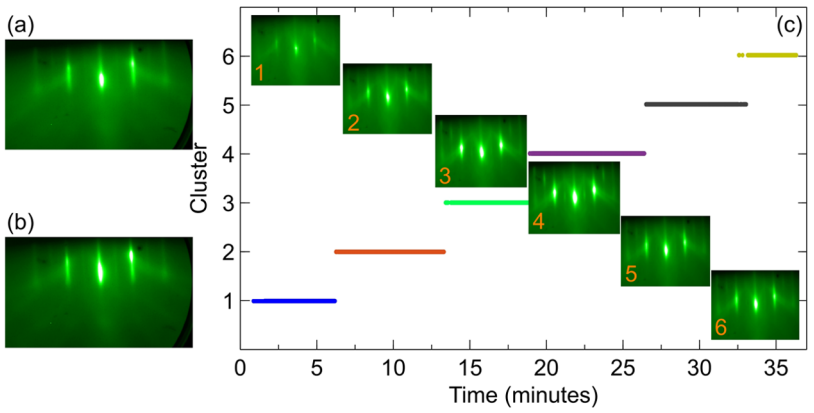

Figure 3. (a) RHEED image of the SHO−TSO film after growth at 1000 °C. (b) RHEED image of the SHO−TSO film after growth at room temperature. (c) *k*-means clustering of the SHO−TSO film. The mean RHEED image for each group is vertically aligned with the group and has the group number inlaid.

Strontium (99.99%, Sigma-Aldrich) was supplied using a low-temperature effusion cell, and the flux was calibrated with a quartz crystal microbalance (QCM). An oxygen environment of 2×10^{-6} Torr was used for calibration. Hf was supplied using the metal−organic precursor tetrakis(ethylmethylamino)hafnium (TEMAH, 99.99%, Sigma-Aldrich). TEMAH was stored in a bubbler and connected to the chamber by an ALD pneumatic valve (Swagelok 316L) and a heated gas injector (E-Science). A capacitance manometer (Baratron) was attached to the gas line to monitor the Hf partial pressure. The temperature of the bubbler was maintained by a heating tape controlled by a PID controller. Hf was calibrated by changing the bubbler temperature and observing the change in the partial pressure. In order to reduce scattering of TEMAH and its constituent molecules during growth, the chamber shroud was cooled to −60 °C using an SP Scientific RC210 pump and Syltherm XLT as the coolant.

Samples were grown using codeposition of Sr and Hf at 1000 °C in an oxygen plasma with a chamber pressure of 2×10^{-6} Torr. Upon opening of the Hf source, the chamber pressure increases to 7×10^{-6} Torr and remains there for the duration of growth. After deposition, the samples were cooled from 1000 to 400 °C over 400 s in an oxygen plasma of 2×10^{-6} Torr. Once the samples reached 200 °C, they were transferred *in vacuo* to the XPS. During growth and cool down, *in situ* RHEED (Staib Instruments) was used to monitor the sample surface and growth quality. Videos of the RHEED were collected using a Flashback Express Recorder. After the growth, principal component analysis and *k*-means clustering were performed on the RHEED using software previously developed by our group.[36]

Characterization. XPS spectra were collected for each sample using a PHI 5400 XPS instrument with a base pressure of 8×10^{-10} Torr. Low-resolution spectra were taken over from 0 to 1400 binding energy (eV) with a pass energy of 178.95 eV, and high-resolution spectra were taken over core-level peaks with pass energies of 35.75 eV. The ratio of cations can be determined through XPS by comparing the areas under the fit curves and adjusting by the ratio of the relative sensitivity factors (RSF). In this way, the stoichiometry of each film was determined. The X-rays were generated by an Al Kα source, and an electron flood gun was used during data collection to prevent electron depletion since the film is not conducting. XPS spectra analysis and curve fitting were done using Casa XPS.

A Rigaku Smartlab XRD instrument with a four-circle goniometer was used to collect $2\theta - \omega$ scans over the (002) peak of each sample. This system utilizes the Cu Kα_1 line isolated with a double bounce Ge (220) monochromator. Reciprocal space maps were captured using a 2D detector and were used to determine the film strain.

Hafnium L_3-edge X-ray absorption spectroscopy was carried out at beamline 20-BM of the Advanced Photon Source at Argonne National Laboratory. The incident X-ray energy was controlled by a Si(111) double crystal monochromator, and the X-ray beam was focused by a Pt/alumina bilayer-coated toroidal mirror. The Hf Lα partial fluorescence yield was collected using a 7-element Ge solid state detector. All samples were spun about an axis normal to the film surface during the measurement to mitigate Bragg peaks. Angles of incidence were maintained under 10°, and the X-ray polarization was oriented either in-plane or out-of-plane. Rotational anisotropy second harmonic generation measurements were performed using an ultrafast light source with an 800 nm wavelength, 50 fs pulse duration, and 200 kHz repetition rate. In the normal incidence geometry, the incident and scattered light were perpendicular to the sample surface. In an oblique incidence geometry, both lights were configured at an angle of ∼15° with respect to the normal incidence geometry. The incident and reflected light were fixed as p- or s polarization, and the reflected SHG intensity is recorded as a function of the azimuthal angle ϕ between the scattering plane (electric polarization) and the in-plane crystalline axis. The incident light was focused onto a 50 μm diameter spot on the sample with a fluence of ∼0.25 mJ/cm^2. The second harmonic signal is collected by a single photon counting EMCCD camera. Calibration figures for SHO films and a comparison with a ferroelectric $BaTiO_3$ reference are shown in Figures S10 and S11, respectively.

Electron Microscopy. The cross section lift-out samples of $SrHfO_3/TbScO_3$ (SHO−TSO) and $SrHfO_3/GdScO_3$ (SHO−GSO) films were prepared using a Thermo Fischer Scientific Helios 5 CX focused-ion beam (FIB)/scanning electron microscope (SEM) DualBeam system at the University of Illinois Chicago. Samples were prepared such that the SHO−TSO sample would have a zone axis of [010] for the orthorhombic TSO substrate, while the SHO−GSO sample had a $[10\bar{1}]$ zone axis for the GSO substrate. This allowed for the observation of cation sublattice and octahedral tilts along both axes to determine the space group of the SHO films under strain. The SHO−TSO and SHO−GSO thin films were sputter-coated with a 10 nm-thick layer of Pt/Pd to avoid charging during FIB lamellae preparation. To protect against the ion-beam-induced surface damage to the SHO films, a protective coating of W was deposited. The final lamellae thinning was performed using a 1 kV ion beam energy to minimize the amorphization of the lamellae cross section and to obtain electron-transparent samples.

Scanning transmission electron microscopy (STEM) experiments were carried out at the University of Illinois Chicago using an aberration-corrected JEOL JEM-ARM200CF microscope. The microscope is equipped with a cold-field emission gun and a CEOS aberration corrector and was operated at 200 kV. The electron energy loss spectroscopy (EELS) experiments were performed using a dual-range Gatan Continuum spectrometer. A spectrometer entrance aperture of 5 mm was used, resulting in a collection semiangle of 53.4 mrad. A dispersion of 0.75 eV per channel was used to acquire the core-loss edges in the low-loss (Sc L and O K) and high-loss (Tb M, Gd M, Hf M, and Sr L) energy range with an acquisition time of 0.25

https://doi.org/10.1021/acsaelm.4c01595
ACS Appl. Electron. Mater. 2025, 7, 983−996

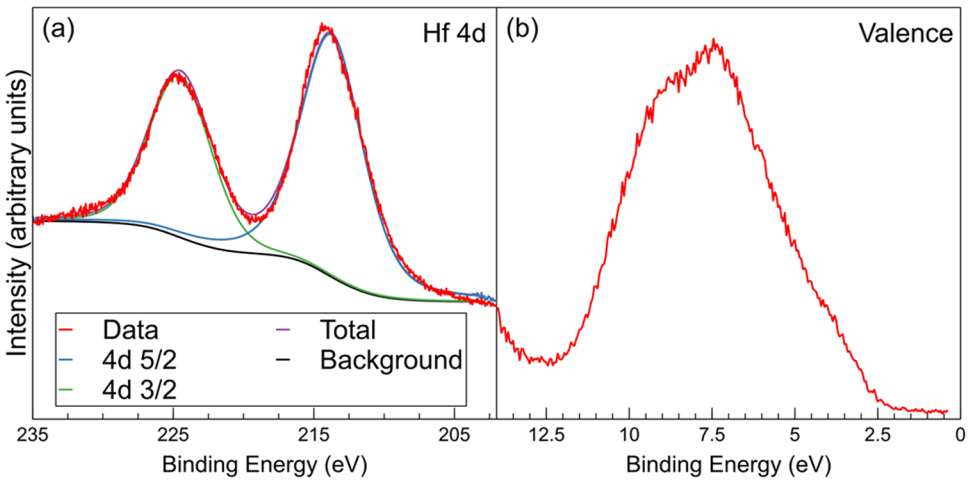

Figure 4. (a) XPS spectra of the Hf 4d peak from the SHO−TSO film. (b) XPS spectra of the valence band of the SHO−TSO film.

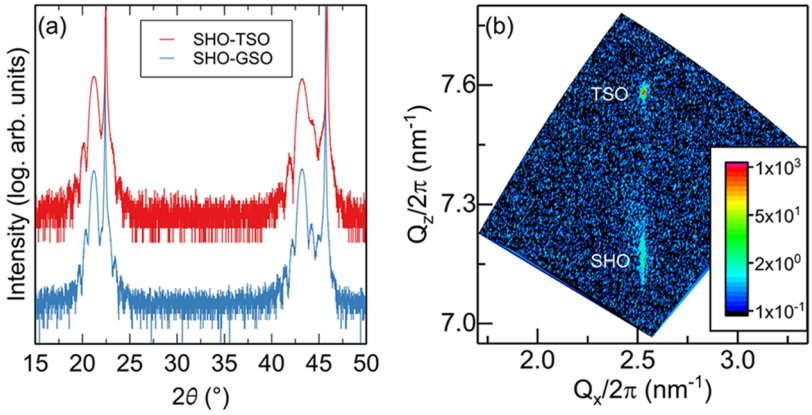

Figure 5. (a) HRXRD of SHO−TSO and SHO−GSO samples. (b) RSM of the SHO−TSO film showing the SHO film is epitaxially strained with TSO.

s per spectrum. The background signal before core-loss edges was modeled by using a power law. To improve the EELS signal quality, principal component analysis (PCA) was performed to remove random noise components. An Oxford X-Max 100TLE windowless silicon drift detector was used to perform energy-dispersive X-ray spectroscopy (EDS).

A probe convergence semiangle of 30 mrad was used to perform atomic-resolution high-angle annular dark-field (HAADF), low-angle annular dark-field (LAADF), and annular bright-field (ABF) imaging. The collection angles used for HAADF, LAADF, and ABF imaging were set to 90−370 mrad, 40−160 mrad, and 11−23 mrad, respectively. The atomic-resolution images were acquired sequentially (10−15 frames). The images were subsequently aligned and integrated to improve the signal-to-noise ratio. For bond-distance analysis, the atomic positions in the HAADF images were initially estimated using the relative intensity. Subsequently, these atomic positions were refined by using 2D Gaussian fitting.

Four-dimensional scanning transmission electron microscopy (4D-STEM) experiments were carried out by using a Gatan ClearView CMOS detector. The microscope was operated at 200 kV with a probe convergence semiangle of 2 mrad. The 4D-STEM data sets were acquired with a pixel size of 0.8−1 nm, and the diffraction patterns were collected using an exposure time of 50−75 ms. A combination of hardware and software binning was used to limit the size of each diffraction pattern to 256 × 256 pixels. The 4D-STEM data analysis was performed using the py4DSTEM Python package.[37]

RESULTS AND DISCUSSION

Film Synthesis and Characterization. Figure 3a shows the high-temperature RHEED image of SHO−TSO along the [110] azimuth immediately following the conclusion of growth, and Figure 3b shows the ambient temperature RHEED image. The bright spots and streaks with clear Kikuchi bands indicate a smooth and highly crystalline surface. The intermediate streaks indicate that a weak surface reconstruction is present. From the *k*-means clustering in Figure 3c, we can see how the surface evolves throughout the 37 min-long growth of SHO−TSO. Each cluster is constructed by minimizing the difference between each frame and the mean frame of the cluster. As a result, each frame in the cluster is most similar to the mean of that cluster than the mean of any other cluster. Cluster 1 encompasses the TSO RHEED pattern and shows a decrease in intensity and softening Kikuchi bands, which is may be attributed to the polar−nonpolar interface and disorder in the early stages of growth. The intensity increases in clusters 2, 3, and 4, with 3 and 4 showing a weak surface reconstruction between the primary spots. This indicates the surface was improving and was highly crystalline and well ordered. The presence of Kikuchi bands in Figure 3b indicates that the surface retains its fairly smooth and retains high crystallinity even after cooling down to ambient temperature.

Figure 4a shows the Hf 4d peak convolutions for SHO−TSO and Figure 4b shows the valence band spectra collected

https://doi.org/10.1021/acsaelm.4c01595
ACS Appl. Electron. Mater. 2025, 7, 983−996

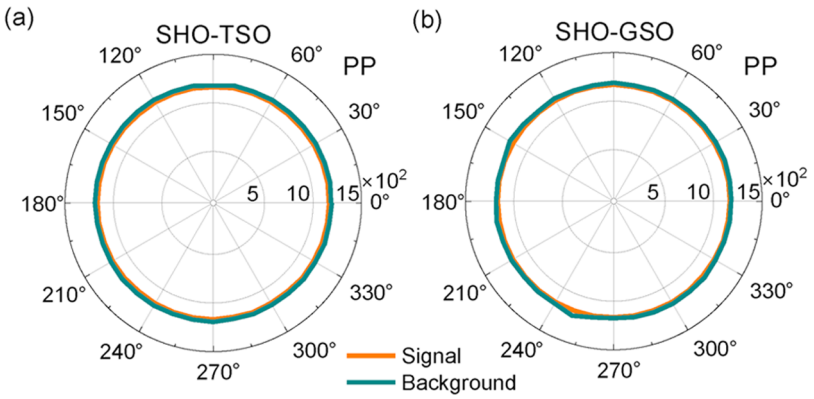

Figure 6. SHG measurements of SHO−TSO (a) and SHO−GSO (b). The lack of significant signal shows that both films are centrosymmetric.

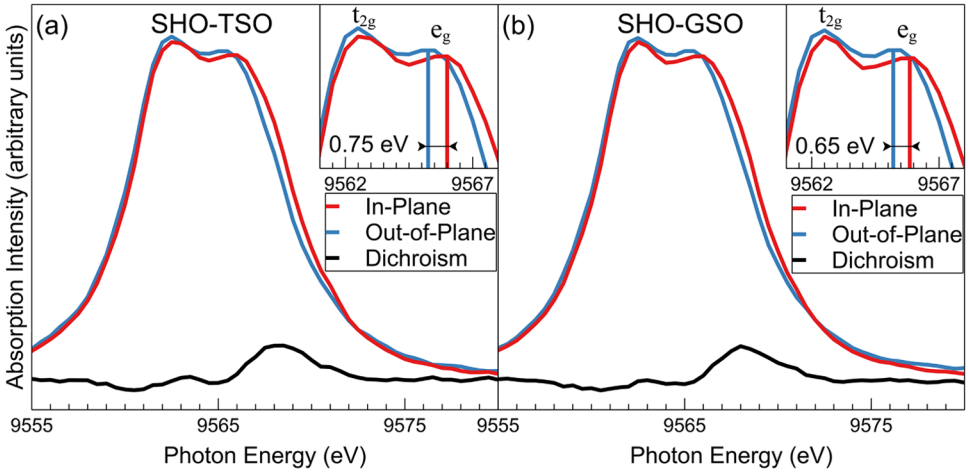

Figure 7. XAS data for SHO−TSO (a) and SHO−GSO (b). Insets show the splitting between in-plane and out-of-plane signals for the e_g band.

at the same time. Peak fits for O 1s and Sr 3d are shown in Figure S7. From the Hf 4d and Sr 3d peaks, the cation ratio of the SHO−TSO sample was calculated to be approximately 1:1, indicating that the film is nearly stoichiometric. Since strontium has a significantly lower atomic mass than terbium, RBS would not provide accurate stoichiometry.

Figure 5a shows the HRXRD spectra of the SHO films grown on TSO and GSO substrates. In both samples, we observe a film peak at lower 2θ values than the TSO and GSO substrate peaks, indicating the films have larger out-of-plane lattice constants. Based on the (002) pseudocubic peaks, the lattice parameters for the films on TSO and GSO are 4.19 and 4.18 Å, respectively. This is in agreement with expectations for elastic deformation due to the greater compressive in-plane strain imparted by the TSO substrate. There are no peaks, indicating other phases are present. Figure 5b shows the reciprocal space map for the (103) pseudocubic peak for the SHO−TSO film. The sharpness of the SHO film peak in the $Q_x/2\pi$ axis indicates that the samples possess a very small range of in-plane lattice constants. The primary SHO film spot and the TSO substrate spot are aligned at the same value on the $Q_x/2\pi$ axis, indicating that the film possesses the same in-plane lattice constant as the substrate and, thus, has a compressive strain of ∼−3%. However, diffuse scattering at smaller Q_x and greater Q_z suggests that there may be some mosaic spread with partial strain relaxation in some parts of the film. Similar RSM data for the SHO−GSO film are shown in Figure S8.

Characterization of Film Space Group. *Second Harmonic Generation.* Figure 6 shows the results of oblique incidence SHG measurements for the SHO−TSO and SHO−GSO samples. Normal incidence measurements to check for in-plane polarization are shown in Figure S9. The results show no sign of a polar response, indicating that the SHO films are centrosymmetric. Of the 5 phases expected for SHO, only the *P*4*mm* phase is polar and noncentrosymmetric. Thus, this result is consistent with the *Pnma*, $Pm\bar{3}$m, *I*4/*mcm*, and *P*4/*mbm* phases of SHO and inconsistent with the emergence of a strain-stabilized *P*4*mm* phase. Models of the expected SHG responses as a function of polar angle are shown in Figure S13. The lack of SHG response also supports the absence of a ferroelectric distortion in strained SHO predicted by previous studies.[11,13] A comparison of SHG measurements for SHO−TSO and ferroelectric $BaTiO_3$ is shown in Figure S11.

The absence of a *P*4*mm* phase is consistent with the DFT modeling presented above which finds that there is a 160 meV/fu difference between the *P*4*mm* and ground-state *Pnma* phases. The absence of a polar phase matches the results found by Acharya et al.,[15] which observed a $Pm\bar{3}m$ phase in SHO films grown on STO by PLD. However, other work[12] found that 35 nm-thick SHO−STO films grown by PLD possessed a *P*4*mm* phase and observed a SHG response. The samples synthesized in these works shown by RSM appeared to be relaxed, as compared to the films presented here, which are compressively strained to the GSO and TSO substrates. Nonetheless, we do not see evidence of a strain-induced polar

https://doi.org/10.1021/acsaelm.4c01595
ACS Appl. Electron. Mater. 2025, 7, 983−996

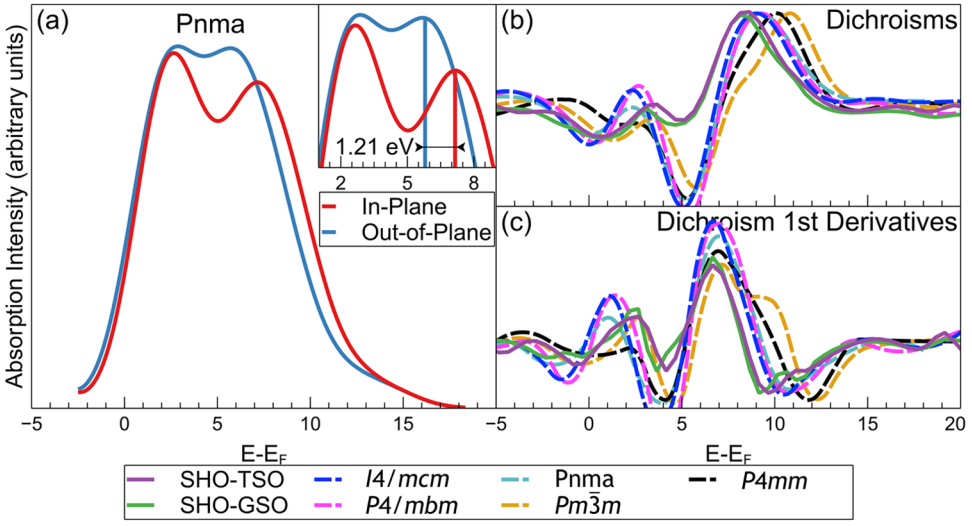

Figure 8. (a) Gaussian convolution of the eDOS from DFT results for the *Pnma* phase of SHO. (b) and (c) The dichroism and it is derivative, respectively, for the XAS data of SHO−TSO, SHO−GSO, and the 5 phases of SHO modeled by DFT with −3% in-plane strain.

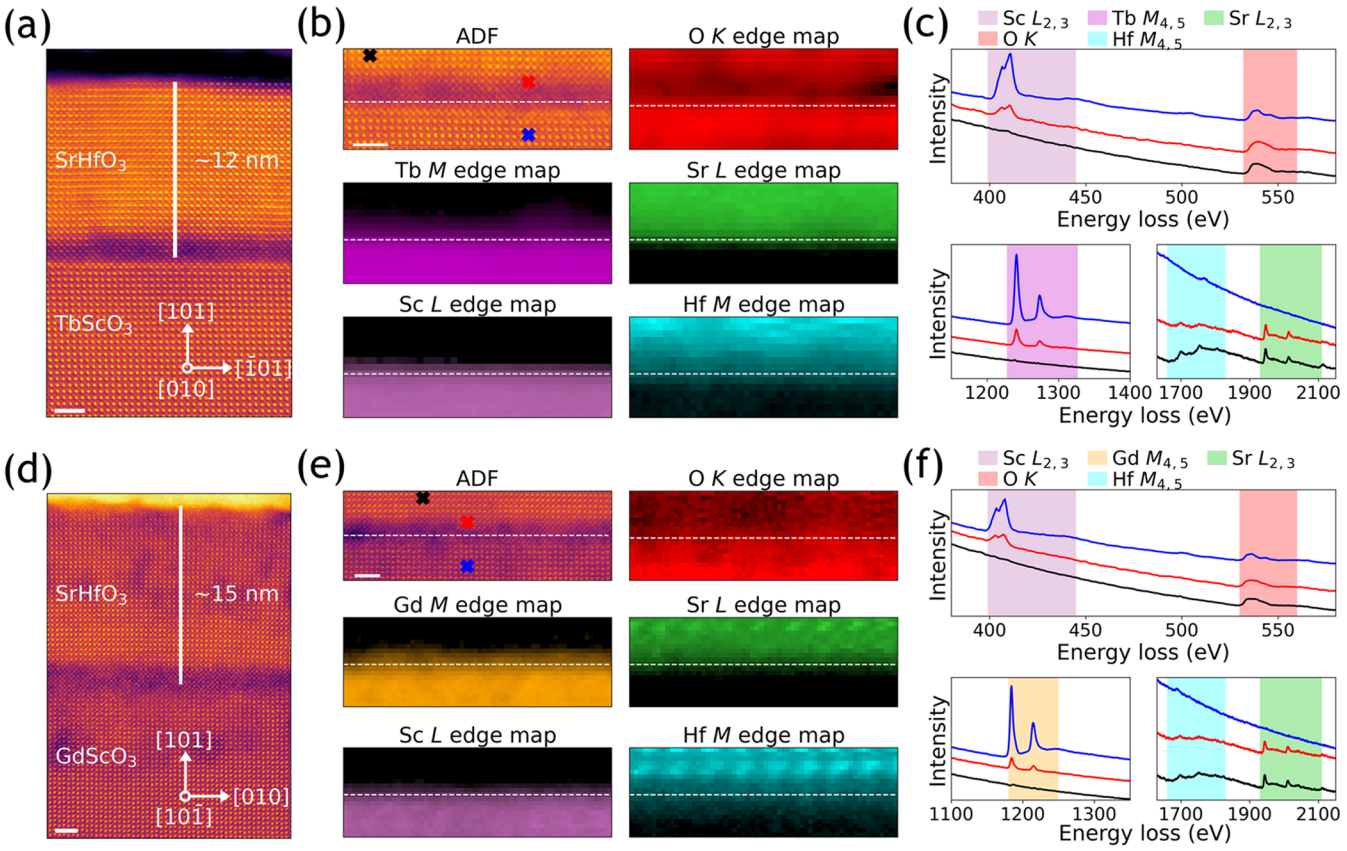

Figure 9. (a) Atomic-resolution HAADF image showing the cross section of the SHO−TSO film along [010]. (b) ADF image along with EELS chemical maps of Tb M, Sc L, O K, Sr L, and Hf M edges across the SHO−TSO interface showing the chemical distribution of elements. (c) Extracted EEL spectra for Tb M, Sc L, O K, Sr L, and Hf M edges. The EEL spectra were extracted from the probe positions marked with the same color in the ADF image shown in (b). (d) Atomic-resolution HAADF image showing the cross section of the SHO−GSO film along [10$\bar{1}$]. (e) ADF image along with EELS chemical maps of Gd M, Sc L, O K, Sr L, and Hf M edges across the SHO−GSO interface showing the chemical distribution of elements. (f) Extracted EEL spectra for Gd M, Sc L, O K, Sr L, and Hf M edges. The EEL spectra were extracted from the probe positions marked with the same color in the ADF image shown in (e). Scale bars in (a), (b), (d), and (e) correspond to 2 nm.

phase, which is consistent with the DFT predictions of phase stability presented above.

X-ray Absorption Spectroscopy. Figure 7a,b depict the Hf L_3-edge for an SHO−TSO film and SHO−GSO film, respectively. These measurements were performed to probe splitting of the energy levels for unoccupied Hf 5d states under strain and to the best of our knowledge are the first reported Hf L_3 spectra for perovskite hafnates. The absorption spectra

https://doi.org/10.1021/acsaelm.4c01595
ACS Appl. Electron. Mater. 2025, 7, 983−996

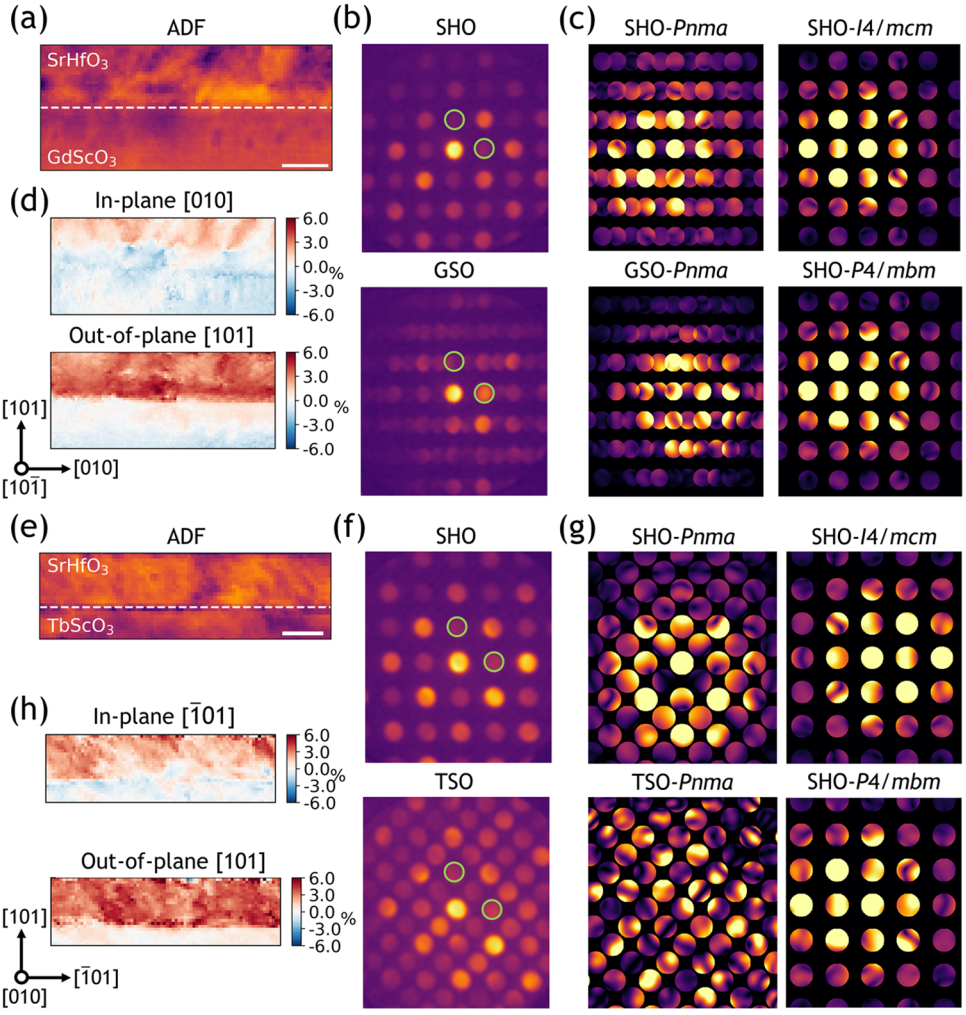

Figure 10. ADF image simultaneously acquired during 4D-STEM data collection for (a) the SHO−GSO and (e) the SHO−TSO samples. The dashed white lines mark the SHO−GSO/TSO interface. CBED patterns for (b) SHO−GSO and (f) SHO−TSO integrated over the area of the film and substrate, respectively. Simulated CBED patterns for (c) SHO−GSO and (g) SHO-−TSO. The crystallographic orientations corresponding to the experimental and simulated data are provided in (d) and (h) for SHO−GSO and SHO−TSO samples, respectively. Strain maps for (d) SHO−GSO and (h) SHO−TSO samples, where strain is calculated with respect to the substrate. Bragg disks used for strain mapping are marked as green circles in (b) and (f) for SHO−GSO and SHO−TSO, respectively. The CBED patterns have been rotated post-acquisition to match the real-space substrate orientation. Scale bars in (a) and (e) correspond to 10 nm.

show clear splitting of the t_{2g} and e_g levels in the absorption, which generally has not been observed in measurements of HfO_2 samples previously.[38] The X-ray linear dichroism (XLD) is calculated by XLD = $I_{ab} - I_c$. In both samples, the t_{2g} peaks are nearly degenerate between the in-plane and out-of-plane response, with the leading edge of the out-of-plane of ∼100 meV. However, the samples exhibit a significantly larger splitting of ∼700 meV between the in-plane and out-of-plane spectra at the e_g peaks. As with the SHG data, the intensity of the dichroism and spectral features for the two samples is quite similar. This suggests that the variation in applied compressive strain from the TSO and GSO substrates does not have a significant impact on the observed properties.

As a result of crystal field splitting, the Hf unoccupied 5d orbitals are broken into t_{2g} and e_g bands where $d_{xz} = d_{yz} = d_{xy} < d_{z^2} = d_{x^2-y^2}$. As observed from the RSM and XRD, these samples are compressively strained in-plane due to the smaller substrate lattice parameter and possess increased c-lattice parameters compared to the bulk. This elastic symmetry-breaking should induce additional crystal field splitting that breaks the degeneracy of the t_{2g} and e_g bands resulting in $d_{xz} = d_{yz} < d_{xy} < d_{z^2} < d_{x^2-y^2}$. This can be observed in the SHO samples by the presence of the weak dichroism in the leading edge and t_{2g} band peak and more substantial dichroism at the e_g peak. This result is consistent with a past study on BTO-$DyScO_3$ (DSO) films, which observed a splitting of ≈1 eV in the e_g band peak, similar to the splitting observed here.[39] While the SHO films exhibit a slight dichroism in the t_{2g} band, the BTO-DSO films observed a triply degenerate t_{2g} band. This degeneracy in the t_{2g} was attributed to the presence of polar distortions, which offset the effect of the crystal field splitting in BTO.[39]

To compare our results with theory, we applied a Gaussian convolution to the eDOS predicted by our DFT calculations to match the XAS instrumental resolution. The resulting convolutions for all 5 phases at −3% compressive strain can be found in the supplement (Figures S13−S15), with the *Pnma* phase shown in Figure 8. As can be seen, all phases except *P4mm* exhibit a positive dichroism on the L_3-edge t_{2g} feature. This dichroism is also exhibited by both SHO samples in

https://doi.org/10.1021/acsaelm.4c01595
ACS Appl. Electron. Mater. 2025, 7, 983−996

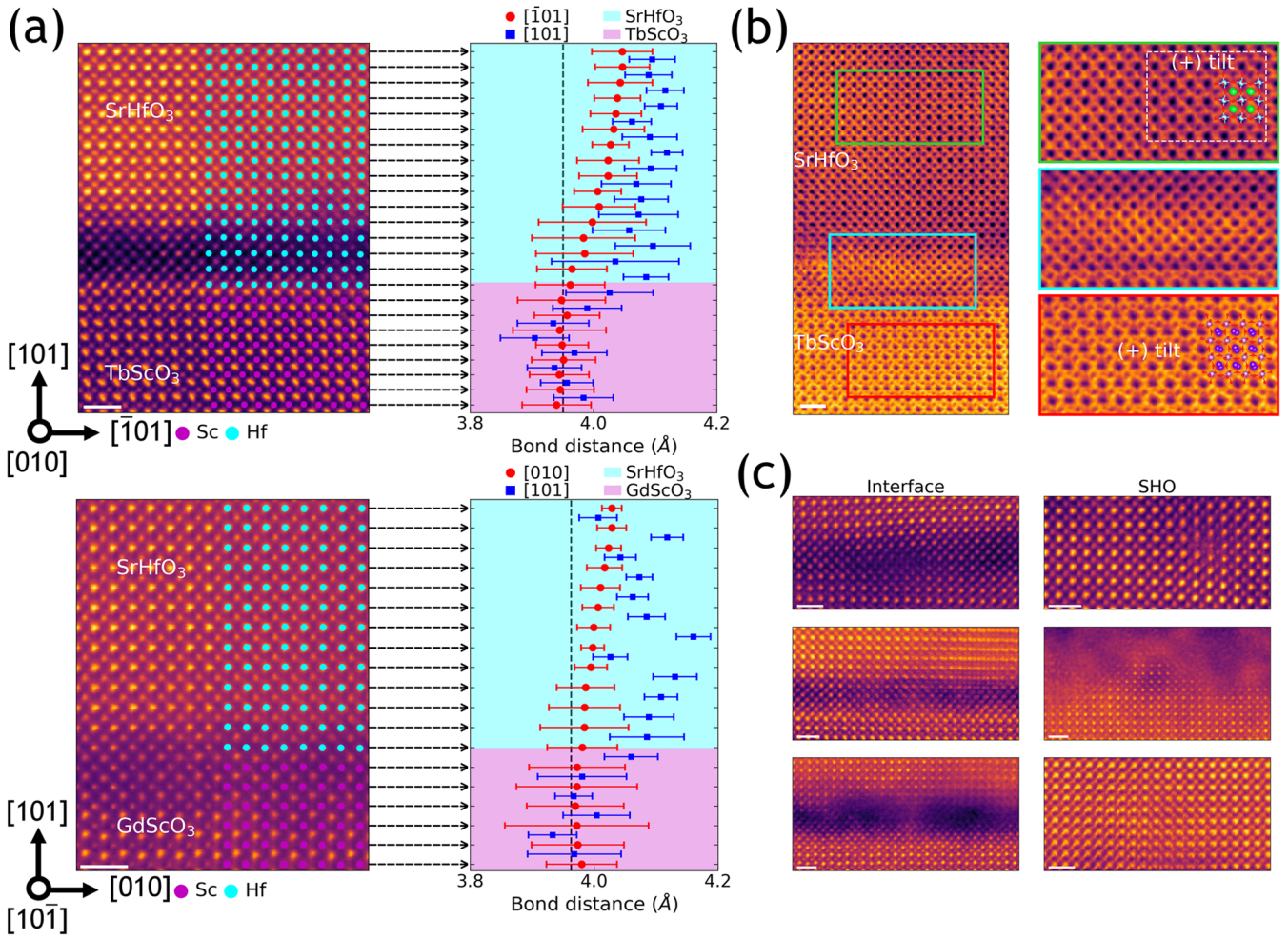

Figure 11. (a) Atomic-resolution HAADF image showing the cross section of SHO−TSO (top) and SHO−GSO (bottom) with labeled B-site cations and the corresponding in-plane and out-of-plane bond distance profiles. The arrows mark the respective atomic planes in the image and the bond-distance plot. The error bars in the bond distance profiles correspond to the standard deviation. The vertical dashed lines mark the in-plane and out-of-plane Sc−Sc bond distances for TSO and GSO, respectively. The crystallographic orientations correspond to that of the TSO and GSO substrates. (b) Atomic-resolution ABF image (left) for an SHO−TSO sample. The higher-resolution ABF images (right) are extracted from the regions marked in same colors as the borders on the left ABF image. (c) Atomic-resolution HAADF images showing defects at the SHO−TSO/GSO interfaces and in the bulk of the SHO films. Scale bars in (a), (b), and (c) correspond to 1 nm.

Figure 7. This result is in agreement with the SHG measurements and effectively rules out the presence of the *P*4*mm* phase. As shown in Figure S10, the $Pm\bar{3}m$ phase possesses an additional feature on the high energy side of the *L*-edge, not present in the other modeled phases or the SHO XANES spectra. In Figure 8b,c, the dichroisms and their derivatives for each phase possess similar features, with the exception of the additional peak on the $Pm\bar{3}m$ phase at 10 eV. These features along with the significant decrease in-phase stability predicted by DFT rule out the presence of the $Pm\bar{3}m$ phase. Determination of the stable octahedral tilt pattern from XAS was not possible due to the very similar XLD predictions for the *Pnma*, *I*4/*mcm*, and *P*4/*mbm* phases.

Scanning Transmission Electron Microscopy. To investigate the atomic and chemical structures of the SHO−TSO and SHO−GSO films along with the interfacial strain effects in the samples, we have performed STEM imaging experiments combined with EELS and EDS. Figure 9 shows the STEM-EELS results for the SHO−TSO and SHO−GSO films. Figure 9a,d show the atomic-resolution HAADF images of the SHO−TSO [010] and SHO−GSO [10$\bar{1}$] films along with their respective crystallographic orientations. We have performed EELS experiments to understand the chemical distribution of elements across the cross section of the SHO−TSO and SHO−GSO. The Sr L, Hf M, Tb M, Gd M, Sc L, and O K edge maps are shown in Figure 9b,e for the SHO−TSO and SHO−GSO thin film samples, respectively. We observed the interface to be chemically diffused for both SHO−TSO and SHO−GSO samples. For instance, on comparing the EELS chemical maps for Tb M and Hf M edges (SHO−TSO) as well as Gd M and Hf M edges (SHO−GSO), we observe the interface is not chemically sharp but diffused. There is formation of a chemically intermixed layer, which is about ≈2−4 unit cells (uc) thick. To emphasize this point, the extracted EEL spectra for different regions of the film and substrate of the SHO−TSO and SHO−GSO samples are shown in Figure 9c,f, respectively. We ascribe this chemical heterogeneity at the interface to nonuniform morphology and surface terminations of the TSO and GSO substrates. Moreover, we also observe the SHO−TSO and SHO−GSO interfaces to be oxygen deficient, as shown in the O K edge maps in Figure 9b,e, respectively. The impact of the chemical

https://doi.org/10.1021/acsaelm.4c01595
ACS Appl. Electron. Mater. 2025, 7, 983−996

heterogeneities at the surface of TSO and GSO substrates on the atomic structure of the SHO films is discussed later in the article. Additionally, the EDS chemical maps for Sr Kα, Hf Lα, Tb Lα, Gd Lα, Sc Kα, and O Kα edges are shown in the Supporting Information, Figure S17.

Our DFT calculations (Figure 2) show that SHO has various energetically competing phases for a range of compressive strains. These phases correspond to *Pnma*, *I*4/*mcm*, *P*4/*mbm*, *P*4*mm*, and *Pm*$\bar{3}$*m*, where *Pnma* is the calculated ground state for a wide range of compressive and tensile strain as shown in Figure 2. The atomic models of the SHO with an in-plane compressive strain of 3% are shown in Figure S1. Both TSO and GSO also adopt the same space-group symmetry of *Pnma* as the calculated ground state of SHO. The atomic models showing the TSO and GSO substrate orientations used for SHO film growth are shown in Figure S2.

To understand the experimental epitaxial relationships between SHO-−GSO/SHO−TSO and evaluate the microstructure of the SHO film, we have performed 4D-STEM experiments. 4D-STEM provides a unique capability of elucidating the space-group symmetry of the sample in reciprocal space with a sufficient real-space resolution to clearly distinguish between the film and the substrate. Figure 10 shows the 4D-STEM results for SHO−GSO [10$\bar{1}$] and SHO−TSO [010]. Figure 10a,e shows the ADF images simultaneously acquired during the 4D-STEM data set collection for SHO−GSO and SHO−TSO, respectively. The extracted convergent-beam electron diffraction (CBED) patterns for the SHO film and GSO/TSO substrates are shown in Figure 10b,f. Figure 10c,g shows the simulated CBED patterns for the SHO-*Pnma*, SHO-*I*4/*mcm*, SHO-*P*4/*mbm*, and GSO-*Pnma*/TSO-*Pnma* phases, along the GSO [10$\bar{1}$] and TSO [010], respectively. By comparing the CBED patterns for the SHO film and the corresponding substrates (GSO and TSO), we can clearly see that the SHO film does not adopt the expected *Pnma* phase. For the SHO film, we find that the simulated CBED patterns for SHO-*I*4*mcm* and SHO-P4*mbm* show a good match with the experimental CBED patterns along both GSO [10$\bar{1}$] and TSO [010] crystallographic orientations. Moreover, simulated kinematical diffraction patterns for parallel electron beam conditions are shown in Figure S18 for all potential SHO phases along with the GSO and TSO substrates.

The diffraction patterns for the *P*4*mm* phase are also within the measurement limits. However, based on the SHG data shown previously, we can rule out the presence of the noncentrosymmetric *P*4*mm* phase. Additionally, we also observe nonorthogonality in CBED patterns between the in-plane and out-of-plane Bragg vectors as well as some very weak reflections, which correspond to small domains with *Pnma* phase in the SHO films, which may be due to strain relaxation and other structural defects in the material. This phase impurity is also consistent with atomic-resolution imaging, described later in Figure 11.

To better understand the microstructure and epitaxy of the SHO films, we further calculated strain for the SHO film using 4D-STEM CBED data. The strain maps for SHO−GSO [10$\bar{1}$] and TSO [010] are shown in Figure 10d,h, respectively. The green circles in Figure 10b,f mark the Bragg disks selected for in-plane and out-of-plane strain calculation. Given that SHO has a larger unit cell volume than the GSO and TSO substrates and the films are grown under a compressive in-plane strain, ≈−3%, we expect a high out-of-plane tensile strain. This can be clearly observed in the out-of-plane strain maps for SHO−GSO and SHO−TSO as shown in Figure 10d,h. The strain maps show nonuniform strain for the in-plane lattice directions for both SHO−GSO and SHO−TSO samples. For perfect epitaxy, the strain along the in-plane direction should be minimal. However, we find that for both samples there are regions that correspond to good epitaxy, but a large fraction of the SHO film shows various degrees of tensile strain along the in-plane direction. The observation of tensile strain along the in-plane direction means that some interfacial strain relaxation has occurred due to misfit dislocations, which can be observed in the HAADF measurements as well. This nonuniformity in strain maps can also be observed in LAADF imaging mode. The LAADF imaging mode is sensitive to strain contrast, where nonuniform image contrast reveals a nonuniform epitaxy and a high density of defects, as shown in Figure S19. Therefore, the nonuniform strain in the SHO films can be directly attributed to phase impurities and a high density of defects arising from the epitaxial mismatch between the film and substrates.

We have further performed atomic-resolution HAADF and ABF imaging to identify the changes in bond distances (Figure 11a), BO_6 octahedral tilt patterns (Figure 11b), and structural defects (Figure 11c) for the SHO−TSO and SHO−GSO samples. Figure 11a shows atomic-resolution HAADF images for the SHO−TSO (top) and SHO−GSO (bottom) samples. Since intensity in a HAADF image is approximately proportional to the squared atomic number (Z^2) of the atomic column,[40] each atomic column in the substrate and the film can be clearly distinguished. For the HAADF images shown in Figure 11a, we labeled the B-site cations (Sc (Z = 21) for TSO/GSO and Hf (Z = 72) for SHO). The HAADF images for the TSO and GSO substrates match well with the expected *Pnma* phase for the substrates along their respective crystallographic orientations. The atomic models for the TSO and GSO substrates are shown in Figure S2. Consistent with the substrate crystallographic orientation (as marked in Figure 11a), we calculated the in-plane and out-of-plane B-site cation bond distances (Sc−Sc for TSO/GSO and Hf−Hf for SHO) using the extracted Sc and Hf atomic positions from the corresponding SHO−TSO and SHO−GSO HAADF images. For the projections shown in Figure 11a, the expected in-plane [$\bar{1}$01] and out-of-plane [101] Sc−Sc bond distance for TSO is 3.95 Å. While for GSO, the expected in-plane [010] and out-of-plane [101] Sc−Sc bond distances are 3.96 Å. These expected Sc−Sc bond distances are marked as vertical dashed lines in the bond distance profiles (Figure 11a).

For an ideal epitaxial relationship, the in-plane bond distances for the film (Hf−Hf) should be constrained to that of the substrate (Sc−Sc) for the entirety of the film thickness, while the out-of-plane bond distance should undergo relaxation (tensile for SHO) as we move further away from the substrate. As shown in Figure 11a, we observe that the calculated in-plane and out-of-plane Sc−Sc bond distances show a good match for both TSO and GSO. We find that the out-of-plane Hf−Hf bond distances are larger compared to that of Sc−Sc, which is expected for the SHO film because of the application of compressive strain by both TSO and GSO substrates. However, for both SHO−TSO and SHO−GSO, we observe that the Hf−Hf in-plane bond distance is not constrained to that of the substrate, i.e., the Sc−Sc in-plane bond distance. This continued relaxation of the in-plane bond

https://doi.org/10.1021/acsaelm.4c01595
ACS Appl. Electron. Mater. 2025, 7, 983−996

distances as we move away from the substrate results in the inability to achieve phase control for the SHO film growth. Moreover, the lack of epitaxial growth constraints results in the growth of SHO films that have a nonuniform interface with a high density of defects (as shown in Figures 11c and S19). We also observe higher error bars in the bond distance profiles close to the interface, which is caused by chemical diffusion at the interface, resulting in the formation of an intermixed layer, as also revealed by STEM-EELS data in Figure 9. The diffused interface along with the high density of defects results in nonuniform strain accommodation as shown by atomic-resolution imaging (Figure 11a) as well as 4D-STEM analysis (Figure 10).

As is the case with most perovskite structures, the BO_6 octahedra can exhibit a variety of tilt patterns, which forms a basis of polymorphism in SHO. To ascertain the HfO_6 octahedral tilt patterns, we have performed atomic-resolution ABF imaging as shown in Figure 11b. We observe that for the TSO substrate, ScO_6 octahedra show the expected (+) tilt pattern along [010] consistent with the TSO-*Pnma* phase. However, for the SHO film, we observe nonuniform octahedral tilt patterns, where some regions exhibit (+) tilt patterns, as shown in Figure 11b, which corresponds to a *Pnma* phase. While some regions do not show any octahedral tilting, which corresponds to pseudocubic [100] and [010] orientations of *I*4/*mcm* and *P*4/*mbm* phases. Consistent with STEM-EELS data as shown in Figure 9, we are unable to resolve the oxygen sublattice in the SHO film at the interface because of a high concentration of oxygen vacancies at the SHO−TSO interface. Moreover, apart from a chemically diffused interface, we also observe a high density of structural defects at the SHO−TSO/GSO interface, as shown in Figure 11c. These defects include dislocations, stacking faults, misorientations, and polycrystalline domains. Additionally, we also observe amorphous domains at the interface as well as at the SHO film surface. This confirms that it is unfeasible for the SHO films to accommodate a high compressive strain beyond a few unit cells. Figure S16 shows wide field-of-view HAADF and LAADF images, where nonuniform strain contrast is evident across the cross section of the SHO films. This further illustrates nonuniform epitaxy and a high density of defects in the SHO films.

Overall, using a combination of STEM-EELS, 4D-STEM CBED, and atomic-resolution imaging, we show that hMBE can yield highly crystalline SHO films on TSO and GSO substrates. However, a high compressive strain results in a diffused interface with a high concentration of oxygen vacancies and structural defects, which makes the phase control of the SHO film extremely challenging.

Discussion. The precise phase control of SHO films using hMBE is extremely challenging because of (1) the various energetically competing SHO polymorphs, (2) high-temperature growth conditions, and (3) a large ≈−3% compressive strain. As described earlier, the perovskite framework allows for the cooperative tilting of HfO_6 octahedra, which means that these polymorphs can readily undergo first- and/or second-order phase transitions.[41] As a result, phase separation in the SHO is likely unavoidable. The ground-state phase for bulk SHO crystals at room temperature is observed to be orthorhombic with a space-group symmetry of *Pnma*, which can undergo phase transitions at higher temperatures.[7] The *Pnma* orthorhombic structure undergoes phase transition to a *Cmcm* orthorhombic structure between 400 and 600 °C. Further phase transition to the *I*4/*mcm* tetragonal structure is observed between 600 and 750 °C. The *I*4/*mcm* tetragonal structure is thermodynamically stable until 1080 °C, beyond which it undergoes phase transition to a cubic $Pm\bar{3}m$ phase. DFT calculations predict the *Pnma* phase to be thermodynamically more favorable than the *I*4/*mcm* phase by 31 meV/fu at −3% compressive strain, as shown in Figure 2. However, the SHO films were grown at a temperature of 1000 °C, followed by cooling down to 400 °C over 400 s, which makes them conducive to adopting the *I*4/*mcm* tetragonal structure. Thermodynamic analysis of the Gibbs free energy of the various SHO phases as a function of temperature and strain is beyond the scope of this work but could help to elucidate whether the *I*4/*mcm* is the equilibrium state at room temperature under these strain conditions or whether it is achieved kinetically through the synthesis approach employed here. Further optimization of growth conditions, such as deposition temperature and prolonged annealing at different temperature ranges, could potentially be a systematic approach to achieve phase control in SHO films grown by hMBE. Additionally, temperature-dependent XRD studies of octahedral tilting in SHO would be valuable to map out the strain vs temperature phase diagram. Such studies would track the half-order diffraction peaks associated with cooperative octahedral tilting and have been performed in other strained perovskite films grown by hybrid MBE.[42]

We observe that the SHO film growth is initially pseudomorphic with respect to the TSO and GSO substrates, as shown in Figure 11. However, such a high compressive strain is eventually unsustainable, resulting in strain relaxation via the formation of a high density of planar defects at the interface, such as dislocations, stacking faults, and polycrystalline domains. The growth of a graded buffer layer could be a potential solution to the high compressive strain issue. A graded buffer layer, with intermediate in-plane lattice parameters in between the substrate and SHO, could help distribute strain gradually. However, the compositional complexity of ternary oxides and the refractory nature of some of the metals make it challenging to identify a suitable buffer layer.

Another critical aspect of phase control of SHO films using hMBE is the quality of substrate, in particular, surface reduction of the substrate prior to growth. As shown by STEM-EELS (Figure 9), the oxygen deficiency at the interface can be explained by the likely reduction of the TSO and GSO before the growth of SHO films. Although the TSO and GSO substrates were heated to 1000 °C for 1 h in oxygen plasma to avoid surface reduction, the ultrahigh vacuum and a high substrate temperature during hMBE could still result in the deleterious reduction of the substrate. This makes the initial ≈−2−4 uc of the SHO layer oxygen deficient, rendering the subsequent growth of the film suboptimal. The development of additional heat and chemical treatment methods for the substrate prior to film growth could potentially alleviate the problem of surface reduction and will be the subject of future work. Recent developments in laser heating of substrates[43] suggest that this approach may be viable to improve the film−substrate interface during growth at temperatures of 1000 °C. This could produce a more well-ordered substrate surface immediately before growth and improve film quality in the future.

https://doi.org/10.1021/acsaelm.4c01595
ACS Appl. Electron. Mater. 2025, 7, 983−996

CONCLUSIONS

We have successfully demonstrated the epitaxial growth of SHO films grown on GSO and TSO substrates using the TEMAH metal organic precursor in hMBE. We have achieved the first synthesis of SHO with −3% biaxial in-plane strain, as confirmed by RSM measurements. Previous DFT studies predicted that SHO films would exhibit the polar *P4mm* phase when synthesized under compressive strain.[11,12] However, SHG measurements identified no polarity in the material, indicating that the samples are centrosymmetric and ruling out the presence of the *P4mm* phase. The absence of polar distortions is in agreement with previous computational studies[13,44] and synthesis experiments.[15] However, this contradicts one previous study that found SHO−STO films exhibited the *P4mm* phase,[12] despite having less experimentally determined compressive strain than the films synthesized in this work.

While DFT modeling showed a small range of structural energies between five possible phases of SHO, XAS measurements and 4D-STEM mapping of the samples rule out the presence of the *Pnma*, *Pm*$\bar{3}$*m*, and *P4mm* phases. The absence of the *Pnma* phase, which SHO, GSO, and TSO take in the bulk, supports previous first-principles studies that predicted compressive strain could change the octahedral tilt pattern in SHO.[13] However, the absence of the cubic *Pm*$\bar{3}$*m* phase contrasts with a synthesis study that found SHO−STO films took on a cubic phase.[15] 4D-STEM measurements showed that the SHO−GSO and SHO−TSO films exhibit *I*4/*mcm* and *P*4/*mbm* phases. Based on the DFT modeling presented, we conclude that the films most likely take on the *I*4/*mcm* structure rather than *P*4/*mbm* due to the 31 meV/fu difference in energy between the two structures. Further support for this phase is based on the bulk phase diagram of SHO, where the *I*4/*mcm* phase is present above room temperature.[7] These results demonstrate that compressive strain tends to drive changes in octahedral tilt patterns in $SrHfO_3$ rather than polar distortions. Future work could examine the temperature dependence of the octahedral tilt patterns through synchrotron XRD measurements or explore ways to synthesize superlattices that drive $SrHfO_3$ into a different phase.

ASSOCIATED CONTENT

Supporting Information

The Supporting Information is available free of charge at https://pubs.acs.org/doi/10.1021/acsaelm.4c01595.

> Additional DFT models assuming other elastic responses in $SrHfO_3$; additional STEM, XAS, XPS, and XRD data; atomic models of various $SrHfO_3$ space groups, along with $GdScO_3$ and $TbScO_3$ structures (PDF)

AUTHOR INFORMATION

Corresponding Authors

Robert F. Klie − *Department of Physics, University of Illinois Chicago, Chicago, Illinois 60607, United States;* orcid.org/0000-0003-4773-6667; Email: rfklie@uic.edu

Ryan B. Comes − *Department of Physics, Auburn University, Auburn, Alabama 36849, United States; Department of Materials Science and Engineering, University of Delaware, Newark, Delaware 19716, United States;* orcid.org/0000-0002-5304-6921; Email: comes@udel.edu

Authors

Patrick T. Gemperline − *Department of Physics, Auburn University, Auburn, Alabama 36849, United States*

Arashdeep Singh Thind − *Department of Physics, University of Illinois Chicago, Chicago, Illinois 60607, United States*

Chunli Tang − *Department of Electrical and Computer Engineering, Auburn University, Auburn, Alabama 36849, United States*

George E. Sterbinsky − *Advanced Photon Source, Argonne National Laboratory, Lemont, Illinois 60439, United States;* orcid.org/0000-0002-1451-5035

Boris Kiefer − *Department of Physics, New Mexico State University, Las Cruces, New Mexico 88003, United States;* orcid.org/0000-0003-0242-3165

Wencan Jin − *Department of Physics, Auburn University, Auburn, Alabama 36849, United States*

Complete contact information is available at: https://pubs.acs.org/10.1021/acsaelm.4c01595

Author Contributions

▽P.G. and A.S.T. contributed equally to this work.

Notes

The authors declare no competing financial interest.

ACKNOWLEDGMENTS

P.T.G. gratefully acknowledges support for synthesis and characterization from the National Science Foundation (NSF) under Award No. DMR-2045993. R.B.C. acknowledges support from the Air Force Office of Scientific Research for the film synthesis and characterization under Award No. FA9550-20-1-0034. W.J. acknowledges support from the US Department of Energy (DOE) Office of Science under DE-SC0023478 and C.T. acknowledges support by NSF EPM Grant No. DMR-2129879. P.T.G. and R.B.C. acknowledge the Auburn University Easley Cluster for support of this work. B.K. gratefully acknowledges the usage of Stampede2 and Stampede3 at TACC through allocation DMR-110093 from the Advanced Cyberinfrastructure Coordination Ecosystem: Services & Support (ACCESS) program, which is supported by National Science Foundation grants #2138259, #2138286, #2138307, #2137603, and #2138296. XRD measurements were performed using an instrument acquired through the NSF Major Research Instrumentation Program under Award No. DMR-2018794. This research used resources of the Advanced Photon Source, a U.S. Department of Energy (DOE) Office of Science user facility operated for the DOE Office of Science by Argonne National Laboratory under Contract No. DE-AC02-06CH11357. A.S.T and R.F.K. were supported by the Office of Basic Energy Sciences, U.S. Department of Energy, Award No. DE-SC0025396. Acquisition of the UIC JEOL ARM200CF was supported by an MRI-R^2 grant from the National Science Foundation (DMR-0959470). The Gatan Continuum GIF acquisition at UIC was supported by an MRI grant from the National Science Foundation (DMR-1626065).

REFERENCES

(1) Ohtomo, A.; Hwang, H. Y. A high-mobility electron gas at the $LaAlO_3/SrTiO_3$ heterointerface. *Nature* **2004**, *427*, 423−426.

(2) Liu, C.; Yan, X.; Jin, D.; et al. Two-dimensional superconductivity and anisotropic transport at $KTaO_3$ (111) interfaces. *Science* **2021**, *371*, 716−721.

(3) Shoron, O. F.; Raghavan, S.; Freeze, C. R.; Stemmer, S. $BaTiO_3$/$SrTiO_3$ heterostructures for ferroelectric field effect transistors. *Appl. Phys. Lett.* **2017**, *110*, 232902.
(4) Haeni, J. H.; Irvin, P.; Chang, W.; et al. Room-temperature ferroelectricity in strained $SrTiO_3$. *Nature* **2004**, *430*, 758−761.
(5) Mulaosmanovic, H.; Breyer, E. T.; Dünkel, S.; Beyer, S.; Mikolajick, T.; Slesazeck, S. Ferroelectric field-effect transistors based on HfO_2: a review. *Nanotechnology* **2021**, *32*, 502002.
(6) Sousa, M.; Rossel, C.; Marchiori, C.; Siegwart, H.; Caimi, D.; Locquet, J.-P.; Webb, D. J.; Germann, R.; Fompeyrine, J.; Babich, K.; Seo, J. W.; Dieker, C. Optical properties of epitaxial $SrHfO_3$ thin films grown on Si. *J. Appl. Phys.* **2007**, *102*, 104103.
(7) Kennedy, B. J.; Howard, C. J.; Chakoumakos, B. C. High-temperature phase transitions in $SrHfO_3$. *Phys. Rev. B* **1999**, *60*, 2972−2975.
(8) Black, K.; Werner, M.; Rowlands-Jones, R.; Chalker, P.; Rosseinsky, M. $SrHfO_3$ Films Grown on Si(100) by Plasma-Assisted Atomic Layer Deposition. *Chem. Mater.* **2011**, *23*, 2518−2520.
(9) Rossel, C.; Sousa, M.; Marchiori, C.; Fompeyrine, J.; Webb, D.; Caimi, D.; Mereu, B.; Ispas, A.; Locquet, J.; Siegwart, H.; Germann, R.; Tapponnier, A.; Babich, K. $SrHfO_3$ as gate dielectric for future CMOS technology. *Microelectron. Eng.* **2007**, *84*, 1869−1873.
(10) McDaniel, M. D.; Hu, C.; Lu, S.; Ngo, T. Q.; Posadas, A.; Jiang, A.; Smith, D. J.; Yu, E. T.; Demkov, A. A.; Ekerdt, J. G. Atomic layer deposition of crystalline $SrHfO_3$ directly on Ge (001) for high-k dielectric applications. *J. Appl. Phys.* **2015**, *117*, 054101.
(11) Shahmirzaee, H.; Mardani, R. Enhancement of piezoelectricity of tetragonal P4mm $SrHfO_3$ under uniaxial stress: A first principle study. *Comput. Condens. Matter* **2018**, *14*, 46−48.
(12) Garten, L. M.; Dwaraknath, S.; Walker, J.; Mangum, J. S.; Ndione, P. F.; Park, Y.; Beaton, D. A.; Gopalan, V.; Gorman, B. P.; Schelhas, L. T.; Toney, M. F.; Trolier-McKinstry, S.; Persson, K. A.; Ginley, D. S. Theory-Guided Synthesis of a Metastable Lead-Free Piezoelectric Polymorph. *Adv. Mater.* **2018**, *30*, 1800559.
(13) Vali, R. Structural phases of $SrHfO_3$. *Solid State Commun.* **2008**, *148*, 29−31.
(14) Amisi, S. First-principles study of structural and vibrational properties of $SrHfO_3$ compared to $SrZrO_3$. *Comput. Condens. Matter* **2019**, *20*, e00383.
(15) Acharya, M.; Banyas, E.; Ramesh, M.; Jiang, Y.; Fernandez, A.; Dasgupta, A.; Ling, H.; Hanrahan, B.; Persson, K.; Neaton, J. B.; Martin, L. W. Exploring the $Pb_{1-X}Sr_XHfO_3$ System and Potential for High Capacitive Energy Storage Density and Efficiency. *Adv. Mater.* **2022**, *34*, 2105967.
(16) Glazer, A. M. The classification of tilted octahedra in perovskites. *Acta Crystallogr., Sect. B* **1972**, *28*, 3384−3392.
(17) Glazer, A. M. Simple ways of determining perovskite structures. *Acta Crystallogr., Sect. A* **1975**, *31*, 756−762.
(18) Thapa, S.; Provence, S. R.; Gemperline, P. T.; Matthews, B. E.; Spurgeon, S. R.; Battles, S. L.; Heald, S. M.; Kuroda, M. A.; Comes, R. B. Surface stability of $SrNbO_{3+\delta}$ grown by hybrid molecular beam epitaxy. *APL Mater.* **2022**, *10*, 091112.
(19) Aeschlimann, R.; Preziosi, D.; Scheiderer, P.; Sing, M.; Valencia, S.; Santamaria, J.; Luo, C.; Ryll, H.; Radu, F.; Claessen, R.; Piamonteze, C.; Bibes, M. A Living-Dead Magnetic Layer at the Surface of Ferrimagnetic $DyTiO_3$ Thin Films. *Adv. Mater.* **2018**, *30*, 1707489.
(20) Caspi, S.; Shoham, L.; Baskin, M.; Weinfeld, K.; Piamonteze, C.; Stoerzinger, K. A.; Kornblum, L. Effect of capping layers on the near-surface region of $SrVO_3$ films. *J. Vac. Sci. Technol., A* **2022**, *40*, 013208.
(21) Zhong, Z.; Hansmann, P. Band Alignment and Charge Transfer in Complex Oxide Interfaces. *Phys. Rev. X* **2017**, *7*, 011023.
(22) Kim, Y. M.; Park, C.; Ha, T.; Kim, U.; Kim, N.; Shin, J.; Kim, Y.; Yu, J.; Kim, J. H.; Char, K. High-k perovskite gate oxide $BaHfO_3$. *APL Mater.* **2017**, *5*, 016104.
(23) Mahatara, S.; Thapa, S.; Paik, H.; Comes, R.; Kiefer, B. High mobility two-dimensional electron gas at the $BaSnO_3$/$SrNbO_3$ interface. *ACS Appl. Mater. Interfaces* **2022**, *14*, 45025−45031.
(24) Thapa, S.; Provence, S. R.; Jessup, D.; Lapano, J.; Brahlek, M.; Sadowski, J. T.; Reinke, P.; Jin, W.; Comes, R. B. Correlating surface stoichiometry and termination in $SrTiO_3$ films grown by hybrid molecular beam epitaxy. *J. Vac. Sci. Technol., A* **2021**, *39*, 053203.
(25) Brahlek, M.; Gupta, A. S.; Lapano, J.; Roth, J.; Zhang, H.-T.; Zhang, L.; Haislmaier, R.; Engel-Herbert, R. Frontiers in the Growth of Complex Oxide Thin Films: Past, Present, and Future of Hybrid MBE. *Adv. Funct. Mater.* **2018**, *28*, 1702772.
(26) Rimal, G.; Comes, R. B. Advances in complex oxide quantum materials through new approaches to molecular beam epitaxy. *J. Phys. D: Appl. Phys.* **2024**, *57*, 193001.
(27) Adkison, K. M.; Shang, S.-L.; Bocklund, B. J.; Klimm, D.; Schlom, D. G.; Liu, Z.-K. Suitability of binary oxides for molecular-beam epitaxy source materials: A comprehensive thermodynamic analysis. *APL Mater.* **2020**, *8*, 081110.
(28) Hausmann, D. M.; Kim, E.; Becker, J.; Gordon, R. G. Atomic Layer Deposition of Hafnium and Zirconium Oxides Using Metal Amide Precursors. *Chem. Mater.* **2002**, *14*, 4350−4358.
(29) Thapa, S.; Paudel, R.; Blanchet, M. D.; Gemperline, P. T.; Comes, R. B. Probing surfaces and interfaces in complex oxide films via in situ X-ray photoelectron spectroscopy. *J. Mater. Res.* **2021**, *36*, 26−51.
(30) Kresse, G.; Furthmüller, J. Efficiency of ab-initio total energy calculations for metals and semiconductors using a plane-wave basis set. *Comput. Mater. Sci.* **1996**, *6*, 15−50.
(31) Kresse, G.; Furthmüller, J. Efficient iterative schemes for ab initio total-energy calculations using a plane-wave basis set. *Phys. Rev. B* **1996**, *54*, 11169−11186.
(32) Perdew, J. P.; Burke, K.; Ernzerhof, M. Generalized Gradient Approximation Made Simple. *Phys. Rev. Lett.* **1996**, *77*, 3865−3868.
(33) Blöchl, P. E. Projector augmented-wave method. *Phys. Rev. B* **1994**, *50*, 17953−17979.
(34) Kresse, G.; Joubert, D. From ultrasoft pseudopotentials to the projector augmented-wave method. *Phys. Rev. B* **1999**, *59*, 1758−1775.
(35) Jain, A.; Ong, S. P.; Hautier, G.; Chen, W.; Richards, W. D.; Dacek, S.; Cholia, S.; Gunter, D.; Skinner, D.; Ceder, G.; Persson, K. A. Commentary: The Materials Project: A materials genome approach to accelerating materials innovation. *APL Mater.* **2013**, *1*, 011002.
(36) Provence, S. R.; Thapa, S.; Paudel, R.; Truttmann, T. K.; Prakash, A.; Jalan, B.; Comes, R. B. Machine learning analysis of perovskite oxides grown by molecular beam epitaxy. *Phys. Rev. Mater.* **2020**, *4*, 083807.
(37) Savitzky, B. H.; Zeltmann, S. E.; Hughes, L. A.; et al. py4DSTEM: A Software Package for Four-Dimensional Scanning Transmission Electron Microscopy Data Analysis. *Microsc. Microanal.* **2021**, *27*, 712−743.
(38) Cho, D.-Y.; Jung, H.-S.; Hwang, C. S. Structural properties and electronic structure of HfO_2-ZrO_2 composite films. *Phys. Rev. B* **2010**, *82*, 094104.
(39) Song, Y.; Liu, X.; Wen, F.; Kareev, M.; Zhang, R.; Pei, Y.; Bi, J.; Shafer, P.; N'Diaye, A. T.; Arenholz, E.; Park, S. Y.; Cao, Y.; Chakhalian, J. Unconventional crystal-field splitting in noncentrosymmetric $BaTiO_3$ thin films. *Phys. Rev. Mater.* **2020**, *4*, 024413.
(40) Pennycook, S.; Jesson, D. High-resolution Z-contrast imaging of crystals. *Ultramicroscopy* **1991**, *37*, 14−38.
(41) Howard, C. J.; Stokes, H. T. Structures and phase transitions in perovskites-a group-theoretical approach. *Acta Crystallogr., Sect. A* **2005**, *61*, 93−111.
(42) Wang, T.; Prakash, A.; Dong, Y.; Truttmann, T.; Bucsek, A.; James, R.; Fong, D. D.; Kim, J.-W.; Ryan, P. J.; Zhou, H.; et al. Engineering SrSnO3 phases and electron mobility at room temperature using epitaxial strain. *ACS Appl. Mater. Interfaces* **2018**, *10*, 43802−43808.
(43) Hensling, F. V. E.; Braun, W.; Kim, D.; Majer, L.; Smink, S.; Faeth, B.; Mannhart, J. State of the art, trends, and opportunities for oxide epitaxy. *APL Mater.* **2024**, *12*, 040902.

(44) Cherrad, D.; Maouche, D. Structural, electronic and optical properties of $SrHfO_3$ (I4/mcm, Imma, Cmcm, P4/mbm and P4mm) phases. *Phys. B* **2010**, *405*, 3862−3868.

https://doi.org/10.1021/acsaelm.4c01595
ACS Appl. Electron. Mater. 2025, 7, 983−996